# Corrections of stratified tropospheric delays in SAR interferometry: Validation with global atmospheric models

M.-P. Doin [a,*], C. Lasserre [b], G. Peltzer [c,d], O. Cavalié [b], C. Doubre [e]

[a] *Laboratoire de Géologie, CNRS UMR 8538, École Normale Supérieure, Paris, France*
[b] *Laboratoire de Géophysique Interne et Tectonophysique, Université Joseph, Fourier, CNRS, BP53 38041 Grenoble Cedex 09, France*
[c] *Department of Earth and Space Science, University of California Los Angeles, CA 10095, USA*
[d] *Jet Propulsion Laboratory, California Institute of Technology, Pasadena, CA, 91109, USA*
[e] *EOST-IPGS (UMR 7516 CNRS-UdS), 5 rue Ren Descartes, 67084, Strasbourg, Cedex, France*

## ARTICLE INFO

## ABSTRACT

The main limiting factor on the accuracy of Interferometric SAR measurements (InSAR) comes from phase propagation delays through the troposphere. The delay can be divided into a stratified component, which correlates with the topography and often dominates the tropospheric signal, and a turbulent component. We use Global Atmospheric Models (GAM) to estimate the stratified phase delay and delay-elevation ratio at epochs of SAR acquisitions, and compare them to observed phase delay derived from SAR interferograms. Three test areas are selected with different geographic and climatic environments and with large SAR archive available. The Lake Mead, Nevada, USA is covered by 79 ERS1/2 and ENVISAT acquisitions, the Haiyuan Fault area, Gansu, China, by 24 ERS1/2 acquisitions, and the Afar region, Republic of Djibouti, by 91 Radarsat acquisitions. The hydrostatic and wet stratified delays are computed from GAM as a function of atmospheric pressure $P$, temperature $T$, and water vapor partial pressure $e$ vertical profiles. The hydrostatic delay, which depends on ratio $P/T$, varies significantly at low elevation and cannot be neglected. The wet component of the delay depends mostly on the near surface specific humidity. GAM predicted delay-elevation ratios are in good agreement with the ratios derived from InSAR data away from deforming zones. Both estimations of the delay-elevation ratio can thus be used to perform a first order correction of the observed interferometric phase to retrieve a ground motion signal of low amplitude. We also demonstrate that aliasing of daily and seasonal variations in the stratified delay due to uneven sampling of SAR data significantly bias InSAR data stacks or time series produced after temporal smoothing. In all three test cases, the InSAR data stacks or smoothed time series present a residual stratified delay of the order of the expected deformation signal. In all cases, correcting interferograms from the stratified delay removes all these biases. We quantify the standard error associated with the correction of the stratified atmospheric delay. It varies from one site to another depending on the prevailing atmospheric conditions, but remains bounded by the standard deviation of the daily fluctuations of the stratified delay around the seasonal average. Finally we suggest that the phase delay correction can potentially be improved by introducing a non-linear dependence to the elevation derived from GAM.

## 1. Introduction

The main limitation of differential radar interferometry (DInSAR) in measuring centimeter ground displacements, apart from coherence loss, comes from unaccounted electromagnetic phase propagation delays in the atmosphere (Zebker et al., 1997; Hanssen, 2001). Atmospheric propagation delays are a geophysical signal affecting every pixel of the radar scene and masking ground motion, and can potentially be modelled and corrected. They limit the measurement accuracy of post- and inter-seismic deformations in the seismic cycle,

transient creep along some fault segments, volcanic deflation or inflation, subsidence induced by mining or fluid extraction, or ground motion due to loading or unloading of the lithosphere by the hydrosphere. Therefore, it is particularly important to devise techniques to improve our understanding of electromagnetic delays in the atmosphere and to mitigate their effects on SAR measurements.

Propagation delays are caused by dispersive effects in the ionosphere and by air refractivity gradients in the neutral troposphere. Ionospheric effects in SAR interferograms have mostly been observed in auroral zones and are more important in L-band than in C-band. They are revealed by azimuth distortions or shifts in SAR images with characteristic distances generally larger than 100 km, except for kilometer scale azimuth streaks (Gray et al., 2000; Mattar and Gray, 2002; Meyer et al., 2006). Air refractivity gradients in the troposphere

---

are first due to the dry air pressure and temperature and, to a lesser extent, to air moisture and condensed water in clouds or rain. The dry air temperature and pressure can be considered as mostly vertically stratified, and thus lead to a large phase delay varying only with elevation in a radar scene. On the contrary, the air water vapor varies both vertically and laterally over short distances, resulting in random patterns in the interferometric phase in addition to a component correlated with elevation. The delay due to clouds amounts to about a millimeter in excess path length, except for cumulonimbus where it can reach half a centimeter (Hanssen, 2001). The total tropospheric delay is often divided into a stratified delay and a turbulent delay for InSAR applications (Hanssen, 2001).

Numerous studies have focused on the quantification and mitigation of tropospheric delays using various approaches. One type of approach is to characterize the statistical properties of phase delay patterns (Goldstein, 1995; Williams et al., 1998; Emardson et al., 2003; Lohman and Simons, 2005), which are used to construct covariance matrices of observables and to separate stochastic noise from ground motion signal. Alternatively, if tropospheric delay patterns are random in time, stacking independent data (Peltzer et al., 2001; Wright et al., 2001; Schmidt et al., 2005) or applying temporal low-pass filtering or smoothing in time series analysis (e.g., Ferretti et al., 2001; Berardino et al., 2002; Schmidt and Bürgmann, 2003) are effective methods to reduce the noise on the observed phase, provided that the ground motion is stationary during the averaging periods. However, these approaches neglect biases due to data sampling and temporally correlated stratified tropospheric delays, as will be demonstrated in this paper.

Other approaches consist in direct corrections of tropospheric delays, either empirical, based on the analysis of the delay to elevation relationship observed in interferograms away from the main deformation areas (e.g., Remy et al., 2003; Taylor and Peltzer, 2006; Cavalié et al., 2007; Elliott et al., 2008), or based on external data. Such data can be collected by ground meteorological stations (pressure, temperature, and humidity) and extrapolated at higher elevations (Delacourt et al., 1998). However, the extrapolation does not take into account strong boundary layer phenomena near the surface, particularly for the humidity. MODIS (MODerate resolution Imaging Spectrometer, Li et al., 2005) or MERIS (MEdium Resolution Imaging Spectrometer onboard ENVISAT, Li et al., 2006a,c) or large network GPS data (Webley et al., 2002; Li et al., 2006b) have also been successfully used to map the lateral heterogeneities in integrated water vapor content from ground to satellite. However, the main limitations of these external data are the often sparse spatial distribution for GPS, the non simultaneity of SAR acquisition with MODIS, and calibration and cloud coverage for MODIS and MERIS. Finally, meso-scale atmospheric dynamic modelling provides a complete mapping of dry and wet tropospheric delays (Wadge et al., 2002; Foster et al., 2006; Puyssegur et al., 2007), but are still limited by weather underpredictability and sensitivity to model boundary conditions.

In this paper, we focus on the quantification and validation of the total *stratified tropospheric delay*. Turbulent patterns in air moisture are prevalent at some acquisition dates, with the occurrence of peculiar atmospheric events. Their effects on InSAR measurement can be decreased by data stacking or time series analysis with appropriate data selection or weighting (Cavalié et al., 2007; Cavalié et al., 2008). Variations in air stratification have a first order effect on all radar acquisitions, with a single path LOS delay reaching ~10 cm/km in some areas. Furthermore, unlike turbulent effects, the sign and amplitude of stratified delays are not random in time due to seasonality, and their spatial patterns are always the same. Stratified delays are therefore less attenuated by stacking or temporal smoothing than turbulent patterns, even when working with a large InSAR data base in the case of a non stationary deformation. Here, we compare the observation of the phase delay stratification in InSAR

data to its prediction from global atmospheric models. These models have the advantage of being available anywhere and at anytime and allow a complete formulation of the dry and wet component of stratified delays. We focus on three study sites in various tectonic and climatic environments (Lake Mead, Nevada, USA, Haiyuan fault, Gansu, China, Afar, Djibouti), where a large SAR data collection is available. After a presentation of the main equations necessary to compute total propagation delays, we demonstrate the feasibility and importance of correcting interferograms from global atmospheric models. We then discuss sampling biases and errors associated with the correction strategies of tropospheric stratified delays.

## 2. Delays in electromagnetic wave propagation

### 2.1. Refractivity and zenith total delay

The air refractivity, $N$, can be expressed as (Smith and Weintraub, 1953; Bean and Dutton, 1968; Thayer, 1974; Hanssen, 2001; Puyssegur et al., 2007):

$$N = k_1 \frac{P_d}{T} + k_2 \frac{e}{T} + k_3 \frac{e}{T^2} + k_4 W_{cl} + k_5 \frac{ne}{f^2} \tag{1}$$

where $P_d$ is the dry air partial pressure in Pa, $e$ is the water vapor pressure in Pa, $T$ is the temperature in K, $W_{cl}$ is cloud water content (in kg/m$^3$), $ne$ is the electron density in the ionosphere and $f$ is electromagnetic wave frequency. The first term corresponds to the effect of dry air on refractivity, the second and third terms are related to air moisture, the fourth is due to the liquid water within clouds and the fifth term is the dispersive effect of ionosphere. The constants in the above formula are $k_1 = 0.776$ K Pa$^{-1}$, $k_2 = 0.716$ K Pa$^{-1}$, $k_3 = 3.75 \times 10^3$ K$^2$ Pa$^{-1}$, $k_4 = 1.45 \times 10^3$ m$^3$ kg$^{-1}$ and $k_5 = -4.03 \times 10^7$ s$^{-2}$ m$^3$.

The zenith excess path $L$ is computed from the integral between the surface elevation $z_0$ and the atmosphere top (at $z \sim \infty$) of the air refractivity $N$:

$$L = 10^{-6} \int_{z_0}^{\infty} \left( k_1 \frac{P}{T} + (k_2 - k_1) \frac{e}{T} + k_3 \frac{e}{T^2} + k_4 W_{cl} + k_5 \frac{ne}{f^2} \right) dz \tag{2}$$

where the dry air pressure $P_d$ in Eq. (1) has been replaced by $P - e$, $P$ being the pressure of moist air. Note that $k_2 - k_1$ is often referred to as $k_2'' = -0.06$ K Pa$^{-1}$. In this paper, we focus on the first three terms of Eq. (2) without further discussing both the delay associated with the cloud liquid water content and the delay due to the ionosphere.

Eq. (2) can then be rearranged, using the state equation for the density of moist air, $\rho$:

$$\rho = \frac{P_d}{R_d T} + \frac{e}{R_v T} = \frac{P}{R_d T} + \left( \frac{1}{R_v} - \frac{1}{R_d} \right) \frac{e}{T} \tag{3}$$

where $R_d$ is the specific gas constant for dry air ($R_d = 287.05$ J/kg/K) and $R_v$ is the specific gas constant for water vapor ($R_v = 461.495$ J/kg/K), and the hydrostatic equilibrium:

$$dP = -\rho g dz \tag{4}$$

leading to (Baby et al., 1988):

$$L = 10^{-6} \left[ \frac{k_1 R_d}{g_m} P(z_0) + \int_{z_0}^{\infty} \left( \left( k_2 - \frac{R_d}{R_v} k_1 \right) \frac{e}{T} + k_3 \frac{e}{T^2} \right) dz \right] \tag{5}$$

where $P(z_0)$ is the surface pressure, $g_m$ is the gravitational acceleration $g$ averaged over the troposphere and $\left( k_2 - \frac{R_d}{R_v} k_1 \right)$ is often named $k_2' = 0.233$ K Pa$^{-1}$. The first term of Eq. (5) is then called the zenith hydrostatic delay (ZHD, ~3.5 m), whereas the zenith wet delay (ZWD,

~30 cm) includes the last two terms that depend explicitly on the water vapor partial pressure $e$ (Davis et al., 1985). This decomposition of the zenith total delay (ZTD) into two terms (ZHD and ZWD) is classically used for GPS tropospheric corrections (Askne and Nordius, 1987; Bevis et al., 1994), where ZHD is assumed to be well constrained from surface pressure measurements and where ZWD is estimated during GPS processing.

In Eq. (5), the surface pressure $P(z_0)$ depends on the local surface elevation $z_0$. It has sometimes been estimated from the pressure at zero elevation, $P(0)$, using a formula of the type (e.g., Delacourt et al., 1998):

$$P(z_0) = P(0)\left(1 - 2.26 \times 10^{-5} z_0\right)^{5.225}. \tag{6}$$

However, this extrapolation of $P$ at higher elevation is not accurate, in the sense that it does not include the effect of temporal temperature variations. A better approximation of $P(z_0)$, assuming hydrostatic equilibrium and dry air density, depends on the surface temperature, $T_s$, and on the temperature lapse rate, $\beta$, in the following way:

$$P(z_0) = P(0)\left(1 - \frac{\beta}{T_s} z_0\right)^{\frac{g}{R_d \beta}}. \tag{7}$$

The temporal variability of $\beta$ and $T_s$ (neglected in Eq. (6)) has a stronger impact than the temporal variability of $P(0)$ on tropospheric corrections for InSAR studies, as shown below. Due to the dry air density approximation, the elevation dependence of $P$ given in Eq. (7) does not include $e/T$. Therefore, using expression (7) to compute the hydrostatic delay in Eq. (5) results in a slight approximation. Note, however, that in all cases (Eqs. (1), (2) and (5)), the term in $\frac{e}{T}$ is very small relative to the term in $\frac{e}{T^2}$.

## 2.2. Tropospheric signal in InSAR data

Atmospheric delays affecting a SAR interferogram are measured as a double difference, both in time and space, of propagation delays from satellite to ground then back to satellite. There is no absolute delay measured by SAR interferometry. It is useful to decompose the atmospheric delays into those due to atmospheric stratification and those due to a laterally variable, "turbulent", atmospheric state (Hanssen, 2001):

$$N(x,z) = \overline{N}(z) + \delta N(x,z) \tag{8}$$

where $\overline{N}(z)$ is the vertical stratification averaged across the image, $\delta N(x,z)$ is the deviation from the average profile, and $x$ is a location on the radar scene.

The single path "turbulent" delay between dates $i$ and $j$ ($\Delta_{ij}$) and two locations $x_0$ and $x_1$ can be written as a double difference:

$$\Delta_{ij}L^t(x_1) - \Delta_{ij}L^t(x_0) = 10^{-6}\Bigg(\int_{z_0(x_1)}^{\infty}\Big(\delta N_j(x_1,z) - \delta N_i(x_1,z)\Big)dz \tag{9}$$
$$-\int_{z_0(x_0)}^{\infty}\Big(\delta N_j(x_0,z) - \delta N_i(x_0,z)\Big)dz\Bigg)$$

where $z_0(x_1)$ and $z_0(x_0)$ are the surface elevations at locations $x_1$ and $x_0$, respectively. The phase delay measured by InSAR (in radian) is projected along Line Of Sight (LOS), and is obtained by multiplication by $(4\pi/\lambda\cos\theta)$, where $\lambda$ is the radar wavelength and $\theta$ is the local incidence angle. The spatial patterns in interferograms due to $\delta N(x,z)$ show, on average over the whole image, no correlation with elevation, because the horizontal mean has been removed from $\delta N(x,z)$. However, the delay associated with $\delta N(x,z)$ may produce some local correlation with elevation, positive and negative in different parts of the radar scene, if, for example, the atmosphere has different water vapor saturations on the winward and leeward sides of a mountain. One can consider that, due to the high variability of turbulent patterns in the atmosphere, the spatial pattern of the turbulent delay is mostly random at each acquisition date and can be removed efficiently by stacking interferograms (Zebker et al., 1997; Peltzer et al., 2001; Lasserre et al., 2007) or in InSAR time series (e.g., Ferretti et al., 2001; Cavalié et al., 2007).

The single path "stratified" delay between dates $i$ and $j$ ($\Delta_{ij}$), and two locations $x_0$ and $x_1$ at elevations $z_0(x_0)$ and $z_0(x_1)$, reduces to:

$$\Delta_{ij}L^s(x_1) - \Delta_{ij}L^s(x_0) = -10^{-6}\int_{z_0(x_0)}^{z_0(x_1)}\Big(\overline{N}_j(z) - \overline{N}_i(z)\Big)dz. \tag{10}$$

The "stratified" delay is therefore not sensitive to the total integrated phase delay from satellite to ground between two radar acquisitions. Temporal variations in the vertical stratification $\overline{N}(z)$ lead to a delay varying with surface elevation (Delacourt et al., 1998; Beauducel et al., 2000). Due to a varying amplitude and sign, the stratified delay should also be attenuated by stacking interferograms or by smoothing InSAR time series. However, it is clearly less efficient than for turbulent delays, as it is not random in time but seasonal, and its spatial pattern always mimics elevation.

In the following, we focus on the mitigation of the "stratified" delay expressed by Eq. (10). Using Eqs. (2) or (5) and (10), the LOS single path atmospheric delay, $\delta L^s_{LOS}(z)$, neglecting refractive bending, varies with elevation for each acquisition date as:

$$\delta L^s_{LOS}(z) = L^s_{LOS}(z) - L^s_{LOS}(z_{ref})$$
$$= \frac{10^{-6}}{\cos(\theta)}\left(\frac{k_1 R_d}{g_m}(P(z) - P(z_{ref})) - \int_{z_{ref}}^{z}\left(\left(k_2 - \frac{R_d}{R_v}k_1\right)\frac{e}{T} + k_3\frac{e}{T^2}\right)dz\right). \tag{11}$$

Here $g_m$ is a weighted average of $g$ between $z_{ref}$ and $z$ and is very close to $g$. $z_{ref}$ is a reference elevation in the scene, usually the average scene elevation if the interferogram unwrapped phase has been defined with a zero mean. By analogy with ZHD and ZWD defined above for GPS applications, we name in the following the first term hydrostatic delay and the second term wet delay. Relation (11) can be estimated directly from global atmospheric models. We can also define the average delay/elevation ratio $S$ between the minimum, $z_{min}$, and maximum, $z_{max}$, elevation in the SAR scene as:

$$S = \frac{\delta L^s_{LOS}(z_{max}) - \delta L^s_{LOS}(z_{min})}{z_{max} - z_{min}}. \tag{12}$$

## 2.3. Input from global atmospheric models

Global Atmospheric Models (GAM), that include assimilation of surface and satellite data, provide meteorological values (such as temperature, water vapor content, winds, …) at the surface and along pressure levels. They allow us to predict the function $\delta L^s_{LOS}(z)$ (Eq. (11)) and the ratio $S$ (Eq. (12)) at any acquisition date. In this study, we include data from three meteorological models, the ERA40 reanalysis (Uppala et al., 2005) and the operational analysis (hereafter called OPERA) from the European Centre for Medium-Range Weather Forecasts (ECMWF), and the North American Regional Reanalysis (NARR, Mesinger et al., 2006) from the National Centers for Environmental Prediction / National Center for Atmospheric Research (NCEP/NCAR).

The ERA40 meteorological reanalysis covers the 1961–2001 time period with 4 time steps per day and a spatial resolution of 1.125°. It includes a stratification based on 23 pressure levels (the lowest levels are 1000, 925, 850, 775, 700, and 600 hPa). Note that some pressure

levels are below the local model surface elevation, in which case the values given by ECMWF are extrapolations.

We include data from the OPERA analysis after 2001, when ERA40 in unavailable. The spatial and temporal resolution are the same, with a stratification based on 21 pressure levels (the lowest levels are 1000, 925, 850, and 700 hPa).

The NARR model is restricted to North and Central America with a grid spacing of 32 km, and covers the time period from 1979 to the present day with 8 daily time steps. It has 29 pressure levels, with a relatively dense stratification at low elevation (1000, 975, 950, 925, 900, 875, 850, 825, 800, 775, 750, 725, 700, and 650 hPa).

We extract from GAMs vertical profiles of temperature, specific humidity, and geopotential height on pressure levels at a given GAM grid point located in the radar scene (chosen at the lowest elevation possible). We assume that the extracted vertical profile $N(z)$ represents the average stratification above the radar scene, $\bar{N}(z)$. The LOS delay in Eq. (11) and the ratio in Eq. (12) are computed for all days during the acquisition period, between maximum and minimum elevations representative of each SAR scene. Note that their temporal variability might differ from the variability of the zenith total delay (ZTD) integrated from ground to the satellite, because the humid and hydrostatic height scales vary temporally.

## 3. Study areas and SAR data sets

### 3.1. General framework

Three study areas, Lake Mead (Nevada, USA), Haiyuan (Gansu, China), and Afar (Djibouti), have been chosen to compare the "stratified" atmospheric delays observed in interferograms and its prediction based on global atmospheric models. In these three areas, the arid or semi-arid conditions allow a good preservation of interferometric coherence (Cavalié et al., 2007; Cavalié et al., 2008; Doubre and Peltzer, 2007). However, these areas differ by their topography and climate and by the type of ground displacement. For the Lake Mead and Haiyuan sites, we use the available ESA archive,

which does not provide a continuous acquisition on every pass of the ERS and ENVISAT satellites (Fig. 1). For the Afar site, we use the Radarsat archive which includes data for almost all passes of the satellite. The interferograms have been produced using the JPL processing software package ROI-PAC (Rosen et al., 2004). The topographic component of the phase has been removed by using the Shuttle Radar Topography Mission (SRTM, Farr and Kobrick, 2000) digital elevation model corrected for the geoid height.

In the case of ERS and Envisat data for the Lake Mead and Haiyuan sites, orbital fringes are removed by using precise orbits provided by DEOS (Scharroo and Visser, 1998). Residual orbital errors and the stratified component of the tropospheric delay (approximated by a linear relationship with a ratio $k$) are separated by adjusting the interferometric phase to:

$$\Phi = ax + by + cxy + d + kz \qquad (13)$$

where $x$ and $y$ are range and azimuth coordinates and $z$ is the local surface elevation. The joint evaluation of $a$, $b$, $c$, and $k$ allows to account for trade-offs between residual orbital errors and the stratified tropospheric delay.

For the Afar study area, large inaccuracies in the Radarsat satellite state vectors required the use of the ROI-PAC procedure which estimates the baseline (orbit separation) from the unwrapped interferometric phase. The phase-elevation ratio $k$ is evaluated on the unwrapped interferogram already corrected from residual orbital fringes.

### 3.2. Lake Mead area

The Lake Mead is a large reservoir lake located between Nevada and Arizona, in the Central Basin and Range close to the Colorado Plateau. The ground deformation in this area is related to water level fluctuations in the reservoir. A previous ground motion measure extracted from InSAR time series analysis showed that sedimentary areas directly adjacent to the lake are inflating as water level increases
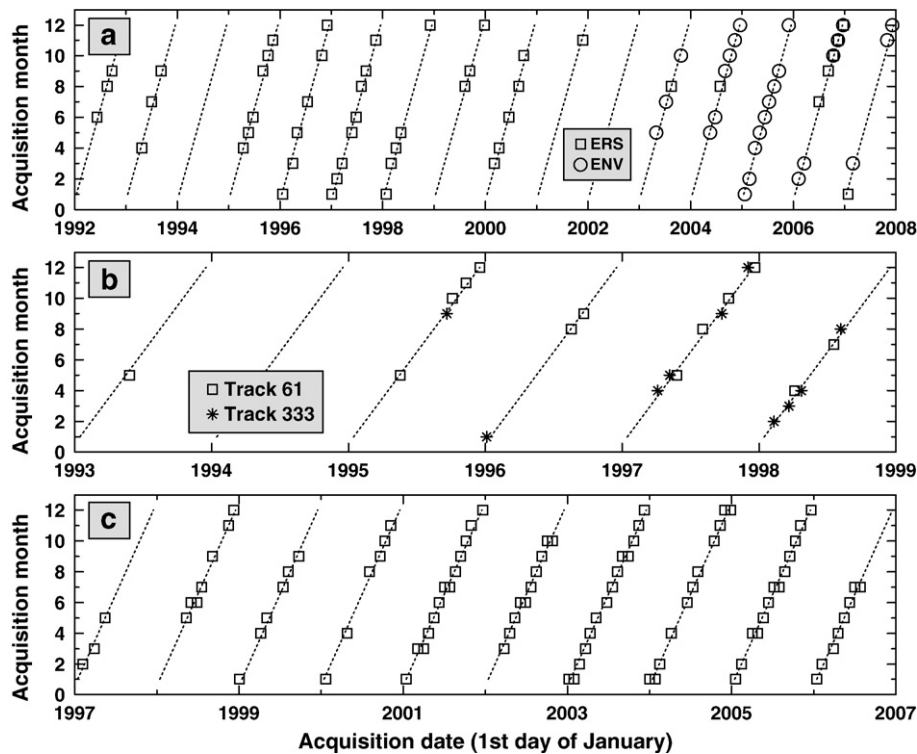


**Fig. 1.** Acquisition dates for (a) 53 ERS and 26 Envisat SAR scenes in the Lake Mead area, (b) 11 ERS SAR scenes on Track 333 and 13 ERS SAR scenes on Track 61 in the Haiyuan area, (c) 94 Radarsat SAR scenes in the Afar area.

and are deflating as water level decreases, probably due to the ground poroelastic response to water infiltration (Cavalié et al., 2007). Furthermore, the water level changes act as a time-varying load on the lithosphere that deflects the ground downwards as water level increases (and inversely), at a wide spatial scale of tens of kilometers. In both cases, peak to peak deformation retrieved from InSAR time series analysis is on the order of 2–3 cm. Because the lake fills a depression, we expect an important correlation between surface deformation and elevation.

The SAR data used in this study include 53 acquisitions by ERS-1 and ERS-2 on descending orbits during the 1992–2007 time period and 26 acquisitions by ENVISAT between 2003 and 2007 (Fig. 1). The acquisition is inconsistent in time, with large gaps between 1993 and 1995 and between 2001 and 2003, and includes several 1-day intervals during the ERS Tandem Mission (from August 1995 to June 1996), and a few 30-minute intervals between ERS2 and ENVISAT passes in 2006. The best seasonal sampling occurs in 2005 with 9 acquisitions. We have formed 413 differential interferograms with perpendicular baselines smaller than 300 m, separately for the two data sets (320 ERS-ERS interferograms and 93 ENVISAT/ENVISAT interferograms). The elevation in the area covered by the data varies from about 300 m on the lake shores to 2000 m on the Colorado plateau on the eastern part of the acquisition scene (Fig. 2a). In many interferograms corrected from residual orbital errors, the phase delay and elevation show a strong linear correlation, as illustrated in Fig. 2a. For all interferograms, we compute the single path LOS delay-elevation ratio $k$ (expressed in cm/km, Eq. (13)) excluding from the fit the main deformation area around the lake.
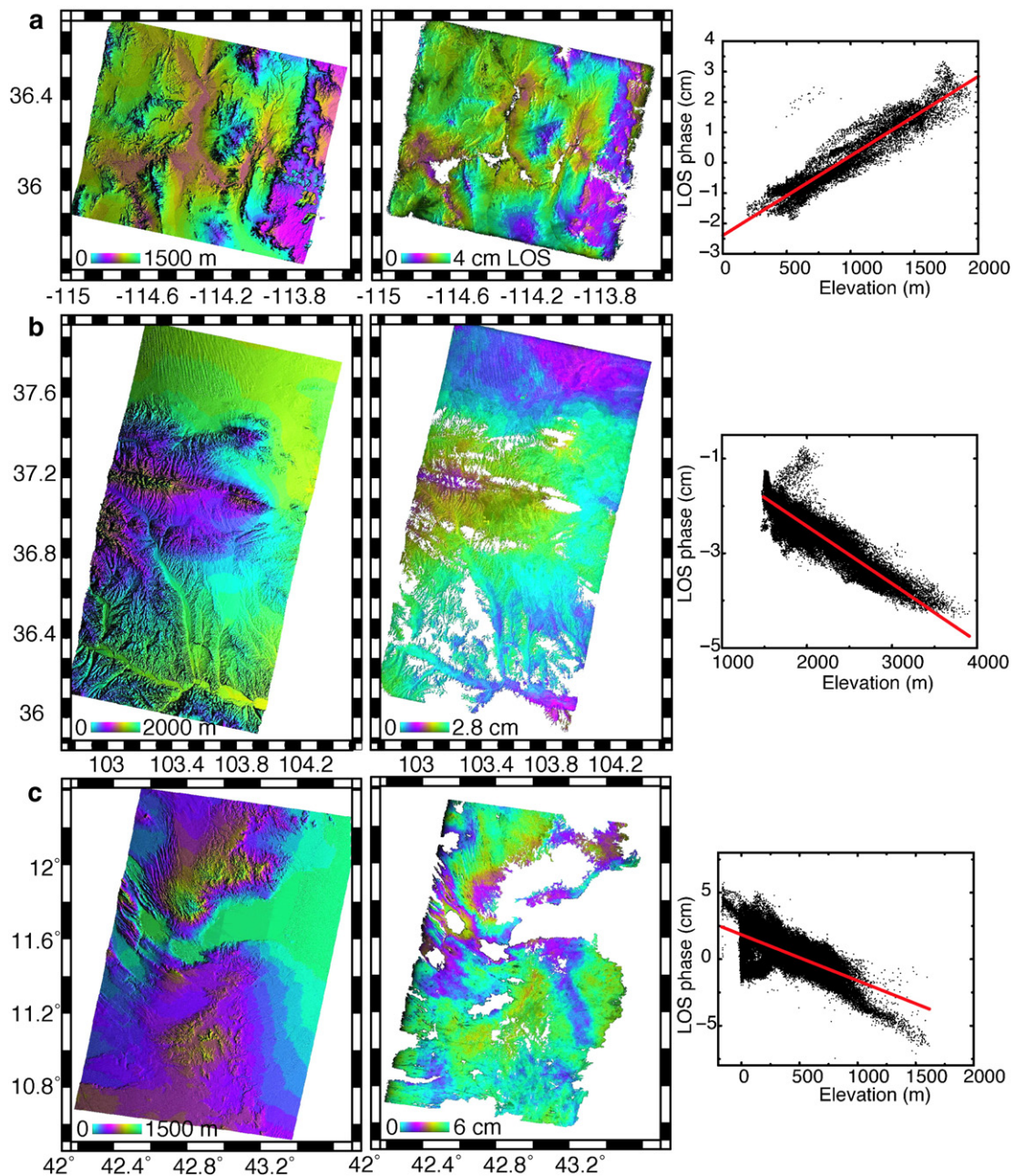


**Fig. 2.** Examples of correlation between interferometric phase (corrected from residual orbital error) and SRTM Digital Elevation Model due to temporal changes in atmospheric stratification. (a): Lake Mead area; (left) SRTM DEM in wrapped colorscale, superimposed on a simulated radar amplitude image; (center) Differential Envisat interferometric phase between 2005/02/27 and 2005/09/25, superimposed on the radar backscatter amplitude; (right) Plot of LOS delay as a function of elevation. (b): As (a) for Haiyuan area along track 333. The tandem ERS differential interferogram is between 1996/01/03 and 1996/01/04. (c): As (a) for Afar area. The Radarsat differential interferogram spans the period 2001/07/04 to 2002/09/09.

The Lake Mead area is characterized by a hot and arid climate affected by wet monsoon episodes during Mid-June to September. Surface (at 2 m) temperature, specific humidity and pressure, together with the total content in water vapor (TCWV) and pressure level data are extracted from NARR at 18 h GMT (whereas the acquisition times for ERS and ENVISAT are 18h18 and 17h50, respectively), at a point of coordinates ($-$114.25 W, 36.375 N) and of model elevation 680 m. The surface temperature varies seasonally from about 8 °C in January to 39 °C in July/August. The surface pressure presents some fluctuations around a seasonal signal of about 12 hPa with a peak in winter. As a result, the ratio $P/T$, which controls the elevation dependence of the hydrostatic delay at low elevation (Eq. (7), Fig. 3a), varies by about 11%, mostly due to temperature variations. In contrast, the ZHD (integrated from ground to satellite) only varies with surface pressure, by ~1.2% (Eq. (5)). The total column water vapor (TCWV), which is the main contribution to the zenith wet delay (ZWD), varies with a relatively clear seasonal signal from about 7.4 kg/m$^2$ in December/January to 30 kg/m$^2$ during the monsoon period. Variations in TCWV can be related to the specific humidity $q_s$ and density $\rho_s$ at 2 m elevation by the humid height scale $H_v = $ TCWV$/\rho_s q_s$. The humid height scale shows seasonal variations from 2000 m in winter to 3700 m in summer. Due to the change in humid height scale, a secondary peak in specific humidity appears in February/March, that does not appear clearly in TCWV. In InSAR data, the wet delay (Eq. (11), Fig. 3b) is dominated by variations of specific humidity (proportional to $e/T$) at low elevation.

Fig. 3 shows the yearly variations of the hydrostatic, wet, and total phase propagation delays integrated between 300 m and 2000 m. To highlight the annual and biannual components of the signal, the following function is fitted to the delays:

$$\delta L^s(z_{min}) - \delta L^s(z_{max}) = A + B \cos(2\pi t + \phi_0) + C \cos(4\pi t + \phi_1) \quad (14)$$

where $t$ is the time in years. Peak to peak amplitude of the hydrostatic delay is consistent from year to year and reaches 3.7 cm. This value is larger than the deformation signal observed in the Lake Mead area ((Cavalié et al., 2007)) and cannot be ignored in analyzing InSAR data. The wet delay shows short-term fluctuations of about 7 cm, super-imposed on a seasonal signal of amplitude ~3.5 cm, with a maximum during the July/October monsoon period and a secondary peak in February and March (Fig. 3b). Part of the hydrostatic and wet delays is out of phase, thus partially cancelling each other. The total delay presents a peak to peak seasonal amplitude of 3.4 cm with large, short-term fluctuations due to the wet component of the delay. The minimum delay occurs in May and is followed by a period of larger delay from July to March, with a maximum in February (Fig. 3c).

### 3.3. Haiyuan area

The Hayiuan fault is located along the northeastern edge of the Tibetan plateau. It is a part of a long fault system, which allows the eastward movement of large crustal blocks (Meyer et al., 1998). The Haiyuan fault accommodates the relative motion between Tibet to the South and the Gobi Ala Shan platform to the North (Gaudemer et al., 1995; Lasserre et al., 1999). The present-day motion is estimated by a previous InSAR study (Cavalié et al., 2008) to be in the range of 4.5 to 8.5 mm/yr, with a deformation concentrated in a narrow, ~20 km-wide, corridor along the fault. In the analysis of the SAR data covering the fault, the trade-off between tectonic motion and phase delay through a stratified atmosphere is expected to be small as the relief across the fault does not correlate with the deformation, although the northern block has, in overall, a slightly lower elevation than the southern block.

ERS data have been acquired on two adjacent, 300 km-long tracks (T061 and T333) (Fig. 1). On track 333, 11 images span the period 1995 to 1998, whereas for track 61, 13 images sample the period 1993 to 1998. The small quantity of data does not provide an even sampling through seasonal cycles. On track 333 the elevation varies between 1500 m and 3500 m. The 25 interferograms computed for this track show an approximately linear phase-elevation dependence, with a negative slope for 20 out of 25. For 14 out of the 25 interferograms, the phase-elevation correlation coefficient is larger than 0.8 (see example in Fig. 2b). On track 61, the elevation varies between 1400 m and 2800 m. The interferograms used for this track show a balanced distribution of positive and negative phase-elevation ratios, but with only 4 interferograms presenting a correlation coefficient larger than 0.8. Such apparent differences for both tracks only result from peculiar SAR sampling and baseline configuration (used to choose small baseline interferograms). For all interferograms across the Haiyuan fault, a model of the ground deformation signal is estimated jointly with the phase-elevation ratio $k$ and the orbital error by including an additional term in expression (14) (Cavalié et al., 2008).

ERA40 model variables, at 2 m and at pressure levels, are extracted at 6 h GMT and at the point of coordinates (37.125 N,104.625E), for
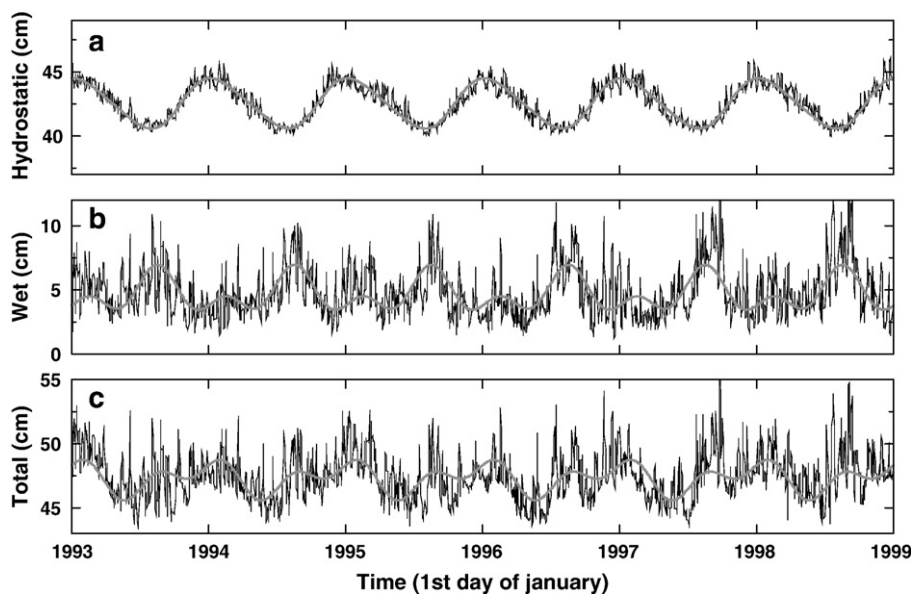


**Fig. 3.** Single path vertical propagation delay from an elevation of 300 m to an elevation of 2000 m ($L(z_{min}) - L(z_{max})$, Eq. (5)) computed using NARR (solid black lines) in the Lake Mead area. (a) Hydrostatic delay, (b) wet delay, (c) total delay. Thick gray lines correspond to seasonal adjustments from 1992 to 2006 using Eq. (14).

which the model surface elevation is 1750 m. The model surface temperature, $T$, increases seasonally from $-3$ °C in January to ~27 °C in July, while the surface pressure, $P$, decreases by approximately 12 hPa between November and July, with large short-wavelength fluctuations around the seasonal curve. The anticorrelation between $P$ and $T$, and more importantly the large $T$ fluctuations, produce large seasonal variations of the hydrostatic delay (Eq. (14), Fig. 4a), which is controlled by the ratio $P/T$. The zenith wet delay, ZWD, is proportional to the integrated water vapor content, TCWV, which has strong seasonal variations peaking around 27 kg/m$^2$ in July and decreasing to around 3 kg/m$^2$ from December to March. The seasonal fluctuations of the InSAR wet delay (Fig. 4b), which is proportional to the specific humidity at the base of the troposphere, are slightly attenuated with respect to ZWD seasonal fluctuations, as the humid height scale $H_v$ varies moderately from 1200 m in winter to 1800 m in summer.

The 3.3 cm, peak to peak seasonal variations in the hydrostatic delay, are in opposite phase with the 6 cm variations of the wet delay, partly canceling each other in the total delay (Fig. 4c). As for the wet delay, the total delay seasonal variations have a maximum in July, with a reduced seasonal amplitude of 4 cm. Large, short-wavelength fluctuations around the seasonal curve, mostly due to the wet component, still remain in the total delay.

### 3.4. Afar area

The third study area covers the eastern part of the Afar depression across the plate boundary between Arabia and Somalia (Fig. 2). East of Lake Asal, the 15–17 mm/yr diverging plate movement is essentially accommodated by normal faulting and opening fissures and dykes across the Asal Rift and continuing into the Gulf of Goubbet (Vigny et al., 2006). The elevation across the rift does not exceed 300 m and remains below sea level around Lake Asal. The relief increases up to 1700 m away from the deforming zone. Therefore, we do not expect any trade-off between tectonic movement and phase delay in interpreting the interferograms, as it may be the case across a strike-slip fault bordering a mountain range (Lasserre et al., 2007).

Radarsat SAR data in standard mode 3 have been acquired since 1997 on almost every descending passes of the satellite. The present data set includes 91 images covering 100 km by 200 km along track 324. In standard mode 3, the LOS incidence angle is 34° in the middle of the swath, larger than that of ERS data (23°) or ENVISAT data in the acquisition mode we used for the Lake Mead area. The return period of Radarsat is 24 days, providing a dense sampling of seasonal changes of the atmospheric phase delay between 1997 and 2006 (Fig. 1). Here we use the series of 427 interferograms processed by Doubre and Peltzer (2007), after averaging them 4 times in range and azimuth. Doubre and Peltzer (2007) inverted the low-resolution interferogram series using the small baseline subset approach (Berardino et al., 2002), applying some temporal smoothing to reduce phase oscillations between epochs of acquisition due to atmospheric propagation delays. In the Asal rift area, phase changes depict the signal from fault movement, rift opening, and volcanic inflation. Away from the rift, the temporal series of the interferometric phase show clear seasonal oscillations, which are interpreted as seasonal atmospheric signal. In many interferograms, the phase shows a strong correlation with elevation (Fig. 2c) but the trend over the full range of elevation is often not as clear as in the other two study areas, probably due to the presence of large bodies of water in the Goubbet Gulf and Lake Asal, defining coastal conditions different from the conditions prevailing inland. Furthermore, the phase-elevation plots show a large dispersion around the stratification trend that can be associated with turbulent atmospheric conditions. Although turbulent atmospheric patterns are also observed in the Lake Mead area data during the monsoon period and in the Haiyuan area data in summer, they are not as large as those observed in the Afar data.

ERA40 model variables, completed by OPERA model variables after 2001, have been extracted at 6 h GMT for a point located at longitude 11.25N and latitude 42.75E, corresponding to a model elevation of 504 m in ERA40 and of 481 m in OPERA. The surface temperature fluctuations from 24 °C in January to 36 °C in June (with a secondary peak in September) are much lower than for the two other sites, while surface pressure varies seasonally by ~10 hPa, peaking in winter. As a result, the ratio $P/T$ which controls the hydrostatic delay varies by only 5% (Fig. 5a). The total column humidity content, TCWV, shows a complex seasonal pattern with a low in December/January (at 17 kg/m$^3$) and a high around 45 kg/m$^3$ during August, with a few secondary humid/dry oscillations in spring and fall. The humid height scale, $H_v$, varies strongly from as low as 800 m in winter to 2200 m in summer. This completely changes the seasonal pattern in the near surface specific humidity with respect to TCWV. As a result, seasonal trends in InSAR wet delays are hardly
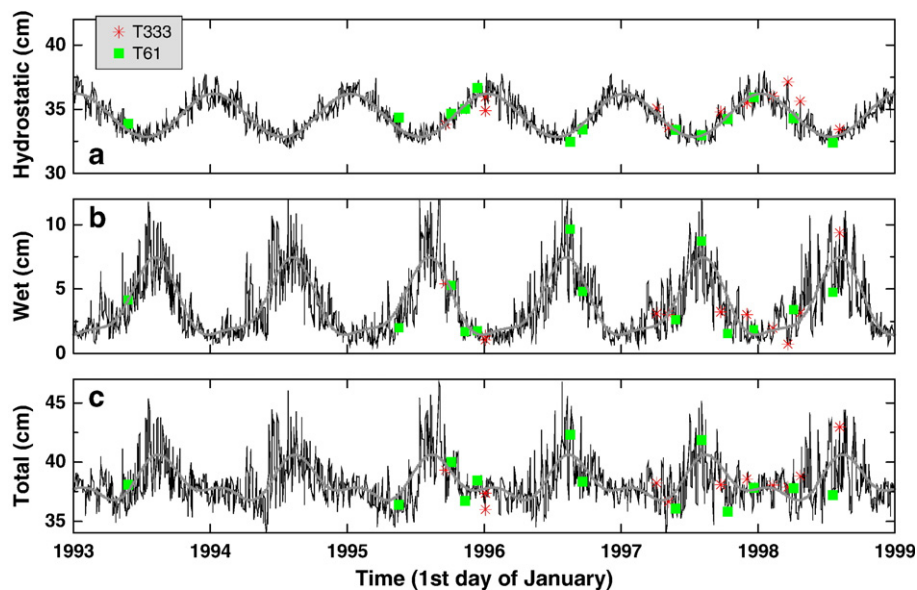


**Fig. 4.** Single path vertical propagation delay from an elevation of 1400 m to an elevation of 3000 m $((L(z_{min}) - L(z_{max})$, Eq. (5)) computed using ERA40 (solid black lines) for the Haiyuan area. (a) Hydrostatic delay, (b) wet delay, (c) total delay. Thick gray lines correspond to seasonal adjustments from 1992 to 2001 using Eq. (14). Symbols are drawn at acquisition times for Track 333 (red stars) and Track 61 (green squares). (For interpretation of the references to color in this figure legend, the reader is referred to the web version of this article.)
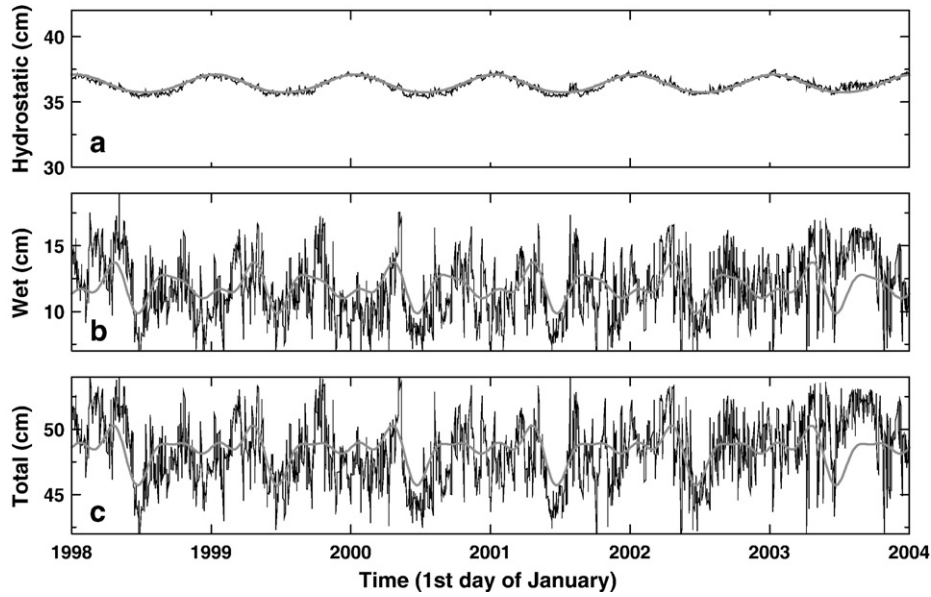
**Fig. 5.** Single path vertical propagation delay from an elevation of 0 m to an elevation of 1500 m (($L(z_{min}) - L(z_{max})$), Eq. (5)) computed using ERA40 followed by OPERA (solid black lines) for Afar area. (a) Hydrostatic delay, (b) wet delay, (c) total delay. Thick gray lines correspond to seasonal adjustments from 1998 to 2007 using Eq. (15).

defined, with a pronounced dry period in June, and a few humidity peaks in October, March, and May (Fig. 5b).

To summarize, the hydrostatic delay (in $P/T$) varies only by 1.5 cm peak to peak, whereas the wet delay seasonal fluctuations are of 3.8 cm with large, short-term fluctuations around the smooth seasonal variations (Fig. 5). To account for the complex seasonal phase delay pattern in Afar, we adjust a time function including 12 months, 6 months, 4 months, and 3 months temporal dependences:

$$\delta L^s(z_{min}) - \delta L^s(z_{max}) = A + B\cos(2\pi t + \phi_0) + C\cos(4\pi t + \phi_1)$$
$$+ D\cos(6\pi t + \phi_2) + E\cos(8\pi t + \phi_3). \quad (15)$$

The total delays shows a well defined low in June, also present both in the hydrostatic and wet delays, and a few highs and lows of lower amplitude between August and May. The amplitude of the seasonal variations of the total delay (~4.2 cm) and of daily fluctuations are higher in Afar than for the two other study areas.

## 4. Stratified atmospheric delays: observations, model predictions and sampling bias

In this section we first compare the stratified atmospheric delay observed in InSAR data with the same quantity estimated using global atmospheric models. This comparison then allows us to discuss and validate various approaches employed for correcting the atmospheric phase delay in radar interferometry data.

### 4.1. Phase / elevation ratio at acquisition dates

The estimated phase-elevation ratio, $k_l$, for a given interferogram $l$ between dates $i$ and $j$, can be written as the difference of ratios $S_i^{SAR}$ and $S_j^{SAR}$ characterizing atmospheric conditions at dates $i$ and $j$. We solve for $S_i^{SAR}$ by inverting the following system of equations for the $N$ interferograms:

$$S_j^{SAR} - S_i^{SAR} = k_l, \quad \text{for } 1 \leq l \leq N$$
$$S_1^{SAR} = 0. \quad (16)$$

A solution can be found provided that any pair of acquisition dates can be connected by a chain of interferograms. This condition is met with the three data sets used in this study, as the few acquisitions that could not be connected to others due to spatial baseline constraints have been discarded from the analysis. Note that ratios $S_i^{SAR}$ actually represent the difference between atmospheric conditions at epochs $i$ and condition at epoch 1, since we set arbitrarily $S_1^{SAR} = 0$ in the calculation. Therefore, when compared to values estimated from atmospheric models, groups of ratios can be shifted by an arbitrary constant.

### 4.2. Comparison of phase/elevation ratios

We compare the relative quantification of stratified atmospheric delays obtained by InSAR, $S_i^{SAR}$, with the absolute delay/elevation ratio predicted from global atmospheric models, $S_i^{MOD}$. To compute $S_i^{MOD}$ (Eq. (12)), we choose the maximum and minimum elevations that bracket the most represented elevation range in the coherent part of the SAR scene.

The comparison is displayed on Fig. 6 separately for the hydrostatic and wet delay for the ERS data set at the Lake Mead area. Neither the hydrostatic nor the wet delay alone well represents the delay/elevation ratios derived from InSAR, as also found in the Althyn Tagh area by Elliott et al. (2008). On the contrary, the total ratios computed from NARR are in very good agreement with SAR derived ratios (Fig. 7a). Therefore, in the Lake Mead area, due to large seasonal temperature fluctuations, the variations in hydrostatic delays cannot be neglected with respect to wet delay variations. The correlation coefficient between $S_i^{SAR}$ and $S_i^{MOD}$ is 0.92 for the ERS data set and 0.86 for the ENVISAT data set. The predicted trend, $S_i^{SAR} = S_i^{MOD} + cst$, falls well within the scattered data points, without any specific adjustment, using the NARR model variables and the electromagnetic constants introduced in Eq. (1). Deviations from the predicted trend can be due to biased estimations of ratio $k$ using SAR data because of turbulent atmospheric conditions, lateral variations in the atmospheric stratification, and trade-off with deformation signal or residual orbital terms. Deviations can also originate in NARR mismodelling of atmospheric processes, in particular in errors in the distribution of the total water vapor content into successive atmospheric layers.

The agreement between SAR derived ratios, $S_i^{SAR}$, and ERA40 derived ratios, $S_i^{MOD}$, is also very encouraging for the two Haiyuan tracks (Fig. 7b). The correlation coefficient is 0.95 for Track 333 and 0.74 for Track 61. The SAR derived ratios, $S_i^{SAR}$, align well along the
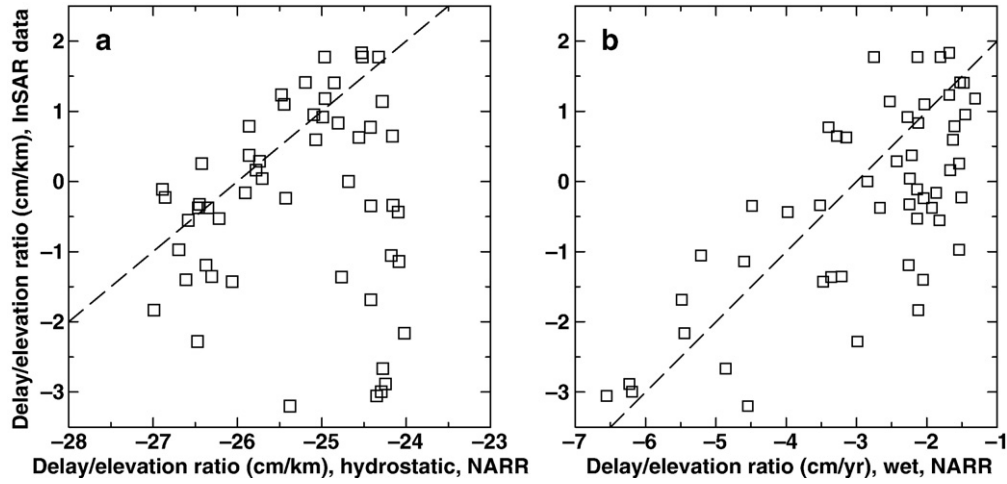
**Fig. 6.** Comparison between delay/elevation ratios derived from InSAR data with those derived from NARR atmospheric model, for all ERS acquisition dates on Lake Mead area: (a) hydrostatic delay prediction. (b) wet delay prediction.

predicted trend, $S_i^{SAR} = S_i^{MOD} + cst$, except for three acquisitions on Track 61. The agreement between SAR derived ratios and ERA40 or OPERA derived ratios is not as good for the Afar study area (Fig. 7c), although the range of delay/elevation ratios is larger in this case ($\pm 4.5$ cm/km) than for Lake Mead ($\pm 2.5$ cm/km) or Haiyuan ($\pm 3$ cm/km). The correlation coefficient between SAR and modeled
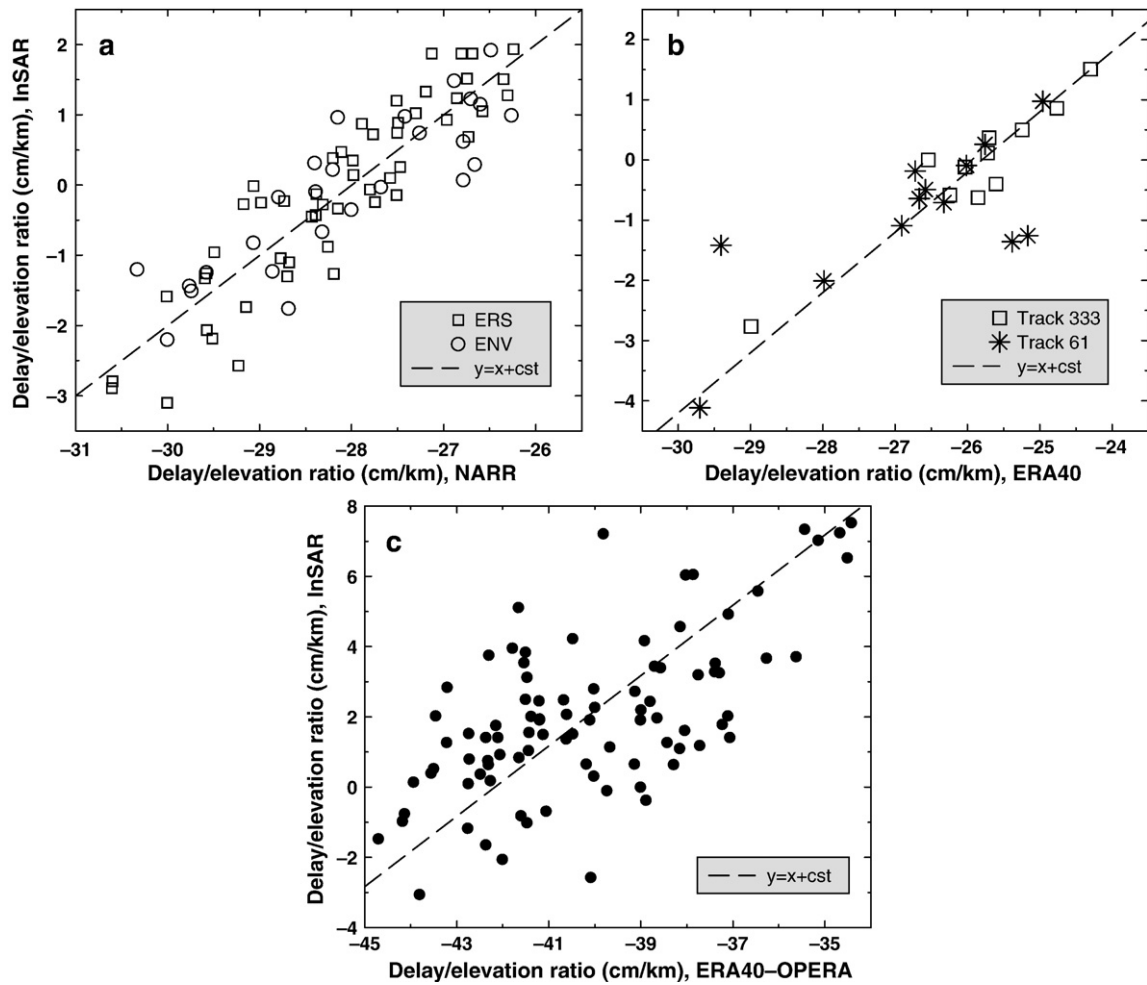


**Fig. 7.** Comparison between delay/elevation ratios derived from InSAR data with those derived from atmospheric models, at SAR acquisition dates. The modeled delay includes both the hydrostatic and the wet terms. The dashed lines $y = x + cst$ correspond to the prediction by atmospheric models with an adjusted constant. (a) Lake Mead area. NARR predictions are integrated between 380 m and 1300 m. ERS and Envisat data sets form two separate groups of delay/elevation ratios which can each be shifted uniformly by an arbitrary constant. The constant for Envisat data is adjusted to follow the same prediction line as ERS data. (b) Haiyuan area. ERA40 predictions are integrated between 1500 m and 3000 m for track 333 and between 1400 m and 2400 m for track 61. The constant for track 61 is adjusted to follow the same prediction line as for track 333. (c) Afar area. ERA40 and OPERA predictions are integrated between 0 m and 1100 m.

ratios is 0.64 for the Afar data. However, it is important to note that even with these noisier data, the predicted trend falls well within the scattered data points. In Afar, the larger deviation between observations and model predictions compared to the two other studied sites comes partly from the more turbulent atmosphere prevailing at low latitude, resulting in a poor phase delay-elevation correlation. The ERA40/OPERA models in Afar area may also be less constrained by meteorological data than the NARR model in the Lake Mead area. The Afar climate, due to turbulences and sea proximity, might also be more difficult to model than the Haiyuan area climate.

### 4.3. SAR data sampling biases and interferograms corrections

In this subsection we show that InSAR measurements of ground motion should be corrected from stratified atmospheric delays or at least be accompanied by error estimations. This is particularly important when the magnitude of the signal is small or may spatially correlate with topography or when the temporal sampling of a SAR data set produces aliasing of atmospheric fluctuations into a low frequency component that could be misinterpreted as ground displacement.

Several approaches are commonly employed to mitigate atmospheric errors in a series of InSAR data. The choice of the approach depends on the sequence of available radar acquisitions and on the ground motion temporal behavior, either linear, or slightly non-linear, or presenting intra-annual or inter-annual fluctuations. These approaches include InSAR data stacking (for linear ground motion and a reduced data set, e.g., Haiyuan site) and temporal smoothing of time series, either over irregular time intervals (for inter-annual ground motion variations and irregular sampling, e.g., Lake Mead site), or over short time intervals (for intra-annual ground motion variations and monthly data sampling, e.g., Afar site). Note that methods applying a low-pass filtering in the time domain (e.g., Ferretti et al., 2001; Berardino et al., 2002) are closely related to smoothing approaches. In all three cases, we first quantify below how the temporal sampling of a SAR data set, that misrepresents daily and seasonal atmospheric fluctuations and may result in an aliased signal at low frequency, biases the retrieved ground motion. Therefore, the extracted ground motions using these approaches are perturbed by

significant residuals in the stratified atmospheric delays, should no stratified delay correction be applied.

We then compare different corrections strategies in removing sampling biases and seasonal effects due to stratified atmospheric delays, depending on the turbulent condition of the atmosphere in the study area: (a) Evaluation of the phase-elevation relationship directly from SAR data, masking off the zones of ground deformation, and correction of the observed phase from the elevation dependent signal. (b) Evaluation of the phase-elevation relationship using atmospheric models, and correction of the interferograms. We show that applying phase delay corrections prior to employing data stacking or temporal smoothing approaches is successful for biases mitigation. Error estimations of the correction applied at each acquisition date will be discussed in Section 4.4.

#### 4.3.1. InSAR data stacking: Haiyuan

In the case of the Haiyuan fault, the inter-seismic velocity (~0.3 cm/yr in LOS) shows a steep gradient across the fault. Due to the small quantity of data acquisitions and in some cases significant turbulent tropospheric delays, Cavalié et al. (2008) chose to stack a selection of interferograms with the largest signal to noise ratio and corrected from stratified tropospheric effects.

Should no stratified delay correction be performed on the interferograms before stacking, what would be the error on fault-slip measurement? To answer this question, we stack the phase-elevation ratios of all interferograms displayed in Fig. 8 and divide by the cumulated duration. Using the phase/elevation ratios derived from InSAR, we obtain 0.07 cm/km/yr for Track 61 and −0.94 cm/km/yr for Track 333. It is strongly negative in the second case as most interferograms have a negative ratio. Therefore, stacking numerous interferograms on Track 333 does not significantly reduce the amplitude of stratified atmospheric delays, which reach ~2 cm/yr for a 2 km elevation range across the stacked velocity map. As, on average, the northern block is ~500 m lower than the southern block, stacking uncorrected interferograms would lead to a bias in the LOS estimated relative block velocity of −0.04 cm/yr for Track 61 and of +0.47 cm/yr for Track 333.

In the Haiyuan study area however, it is relatively easy to estimate separately the deformation from stratified tropospheric delay, as both
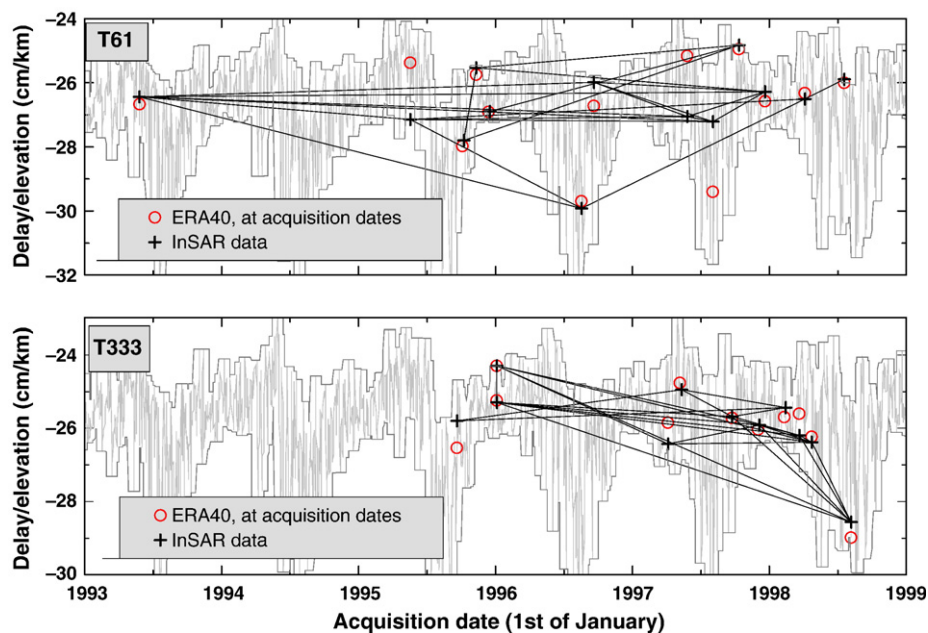


**Fig. 8.** Delay/elevation ratios plotted as a function of time for Haiyuan area. The time series obtained using ERA40 (between 1500 m and 3000 m for track 333 and between 1400 m and 2400 m for track 61) (light gray line) together with enveloppes of monthly minimum and maximum values (dark grey lines) are displayed in the background. Open red circles and black crosses, as in Fig. 9. Links between black crosses show the computed interferograms. (For interpretation of the references to color in this figure legend, the reader is referred to the web version of this article.)
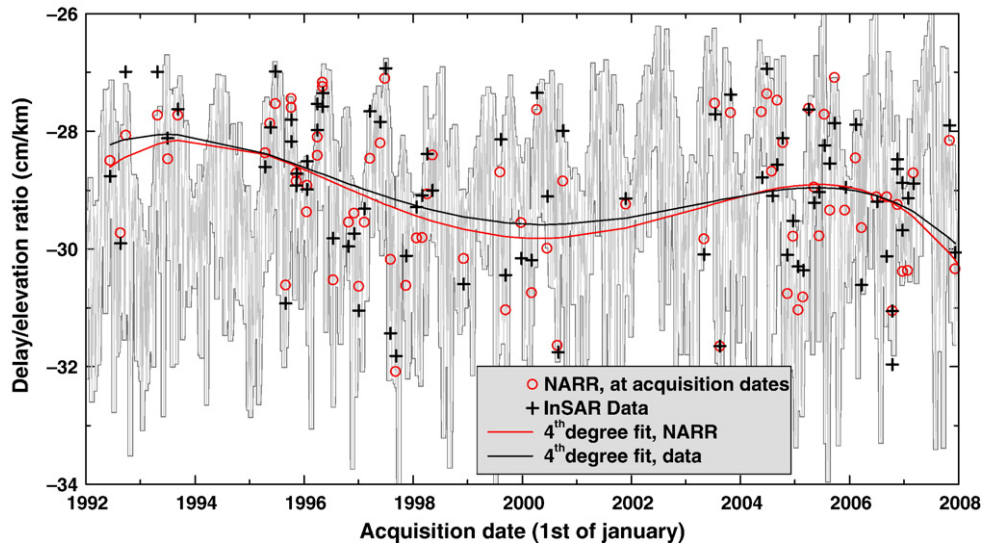
**Fig. 9.** Delay/elevation ratios plotted as a function of time for Lake Mead area. The time series obtained using NARR between 380 m and 1300 m (light gray line) together with enveloppes of monthly minimum and maximum values (dark grey lines) are displayed in the background. Open red circles and black crosses are the NARR predictions and the InSAR delay estimates, respectively. Aliasing due to an uneven sampling through time of high/low delay/elevation ratios is outlined by a 4th degree polynomial adjustment to the sampled NARR predicted values (black line) and InSAR data (red line). (For interpretation of the references to color in this figure legend, the reader is referred to the web version of this article.)

fields are largely spatially uncorrelated. This is a posteriori validated by the very good agreement between ERA40 predictions and measured SAR ratios (Fig. 7). The difference between the stack of ERA40 predicted ratios and the stack of InSAR derived ratios amounts to −0.19 cm/km/yr for Track 61 and to 0.06 cm/km/yr for Track 333. In this case, performing atmospheric corrections using either predicted or measured delay-elevation ratios yields consistent results as the estimated fault velocities would differ by less than 0.1 cm/yr.

### 4.3.2. Temporal smoothing over long time intervals: Lake Mead

In the Lake Mead area, during the period 1992–2007, the interannual water level fluctuations, with peak to peak amplitude of ~20 m, are expected to induce ground movement fluctuations with peak to peak amplitude of ~3 cm. These fluctuations are irregularly

sampled by SAR acquisitions. In this case, the chosen approach is to separate ground motion from atmospheric delays by temporal smoothing of InSAR time series (Cavalié et al., 2007). However, as the deformation is expected to present some correlation with elevation, we must quantify how the stratified atmospheric delay is effectively removed by smoothing.

Fig. 9 shows the aliasing of the stratified delay due to an incomplete sampling by the ERS and Envisat satellites. In this figure, we display how SAR acquisitions sample days of high or low delay-elevation ratio: Between 1992 and 1996, the majority of acquisitions occurs on days with high delay-elevation ratio; Between 1997 and 1999, more acquisitions occurs on days of low ratio; The sampling appears to be more balanced between days of high and low ratios after 1999 although unevenly distributed in time. As a result, when we fit
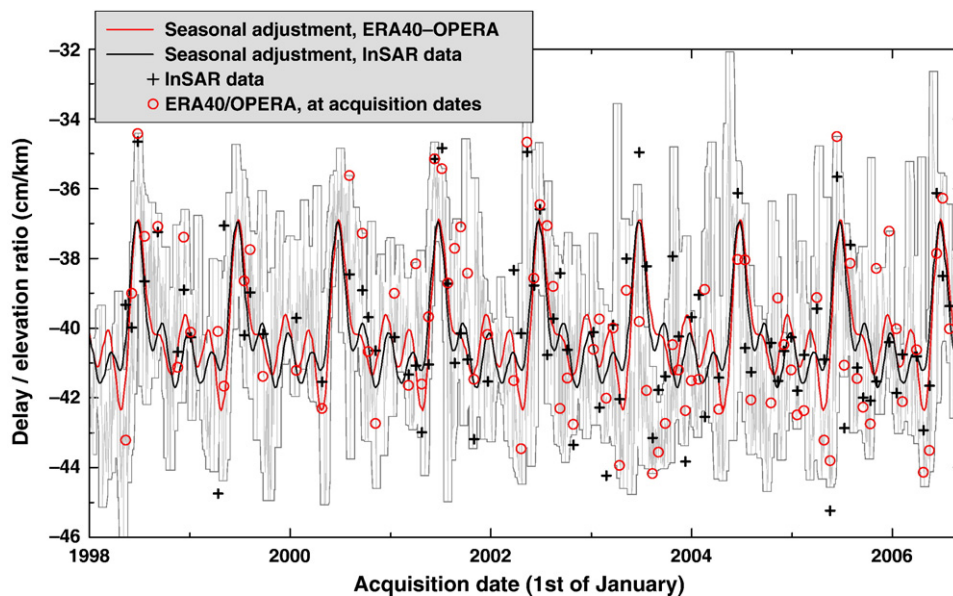


**Fig. 10.** Delay/elevation ratios plotted as a function of time for Afar area. The time series obtained using ERA40 followed by OPERA (between 0 m and 1500 m) together with enveloppes of monthly minimum and maximum values (dark grey lines) are displayed in the background. Open red circles and black crosses, as in Fig. 9. Seasonal adjustments (Eq. (15)) of estimated ratios from InSAR (black line) agrees well with the seasonal delay pattern predicted by the complete ERA40/OPERA time series (red line). Note that these seasonal curves are equally consistent to that derived from the atmospheric model data sub-sampled at radar data acquisition dates (not shown). (For interpretation of the references to color in this figure legend, the reader is referred to the web version of this article.)

the sampled ratios with a 4th order polynom in time, roughly representing the effect of a strong temporal smoothing or low-pass filtering of the data series, we obtain inter-annual fluctuations of 2 cm/km in peak to peak amplitude. The fit is consistent whether using the SAR derived ratios or those estimated from the NARR model. We conclude that in the case of the Lake Mead data, the ground motion retrieved from uncorrected interferograms, after temporal smoothing and even for a long smoothing time interval, would be affected by an error larger than 2 cm in LOS between the lake border and the surrounding mountains (~1 km higher). This error would blur the deformation signal associated with loading.

In the analysis reported in Cavalié et al. (2007), the phase-elevation ratios are estimated from interferograms away from the main deformation area and then used for interferogram correction before being included in the time series analysis.

This stratified delay correction strategy is validated by the good agreement between the smoothed -long-term- trends in phase/elevation ratios derived from InSAR or from NARR (Fig. 9). This shows that correcting interferograms from stratified delays derived from InSAR data or from NARR is sufficient to remove aliasing bias in time series analysis.

### 4.3.3. Temporal smoothing over short time intervals: Afar

In the Afar study area, the smoothed InSAR time series inverted from uncorrected interferograms show a seasonal signal with an amplitude scaling with the elevation (Peltzer and Doubre, 2007). This can be explained by residual stratified atmospheric delays, that are not removed by temporal smoothing. Indeed, Fig. 10 shows that the seasonal fluctuations of the delay-elevation ratio, modeled by function (15) adjusted either to InSAR data or to GAMs data, are consistent. This

suggests that the 24-day repeat sampling along the time axis is sufficient to capture the seasonal atmospheric signal despite the large short-term fluctuations observed is this sub-tropical region. Furthermore, although InSAR observations do not fit well the atmospheric model predictions of the stratified delay at acquisition dates (Fig. 7c), seasonal climate variations estimated from SAR data are consistent with those derived from atmospheric models. We conclude that correcting interferograms from stratified delays derived from SAR data or atmospheric models should remove the seasonal atmospheric signal observed in smoothed InSAR time series, together with possible aliasing bias.

### 4.4. Error analysis on delay/elevation ratios

We discuss below the errors on delay/elevation ratios, either observed from InSAR data or predicted from atmospheric models. The aim is to provide insights on the choice of interferogram correction strategies and to give an error distribution of the stratified delay correction. The correction errors applied at each acquisition date could then be combined to determine the error on the ground motion final result, obtained after data stacking or temporal smoothing.

The quantification of delay/elevation ratios from interferograms is prone to errors, due to (a) trade-offs with residual orbital errors or deformation, (b) lateral variations in stratification, and (c) turbulent atmospheric delays. These errors may influence differently the interferograms, depending on the coherence distribution with elevation (in mountainous areas, for example), or on the SAR data combination (images with or without strong turbulent atmospheric patterns). As a result, the delay/elevation ratios inverted at each acquisition date, $S_i$, do not perfectly fit the redundant set of delay/
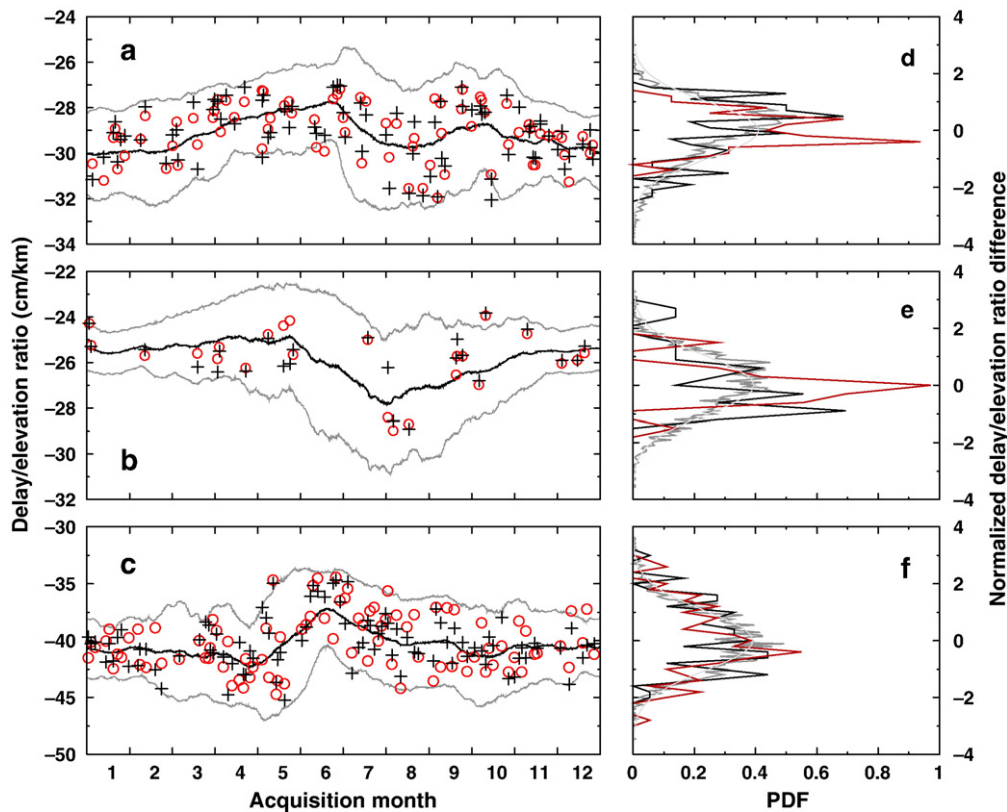


**Fig. 11.** Statistical error analysis of phase/elevation ratios, estimated from InSAR data, $S_i^{SAR}$, or derived from atmospheric models, $S_i^{MOD}$. (a, b, c), for Lake Mead, Haiyuan, and Afar areas, respectively: Delay/elevation ratios plotted as a function of month. The daily prediction averaged over half-month (thick black line) is bracketed by the $2*\sigma(s)$ lines (in gray), where $\sigma(s)$ is the standard deviation of daily predicted ratios over half-month. Open red circles and black crosses: as in Figs. 9 and 10. (d, e, f): probability distribution function for phase/elevation ratios normalized by $\sigma(s)$ (see text). We compare PDF$_2$ of daily predicted ratios minus the seasonal average (grey line), with PDF$_1$ of InSAR derived ratios minus the seasonal average (black line), and PDF$_3$ of InSAR derived ratios minus the predicted ratio at acquisition date (dark red line).

elevation ratios estimated from individual interferograms, $k_l$. The overall misclosure of system (16) provides a minimum error on InSAR derived delay/elevation ratios. That is ~0.2 cm/km for the Lake Mead and Haiyuan test sites and ~0.4 cm/km for the Afar test site. This minimum error is lower than the standard deviation between observation and prediction (~0.55 cm/km, ~0.77 cm/km, and ~2.0 cm/km, for Lake Mead, Haiyuan and Afar test sites, respectively, Fig. 7). One important observation is that, for the three study areas, all InSAR derived ratios fall within or close to the monthly enveloppes of the predicted ratio daily fluctuations (Figs. 8–10).

Errors in the delay/elevation ratios predicted from global atmospheric models may also result from the mismodelling of the water vapor stratification, which may be in part related to the lack of data used for assimilation. Water vapor is indeed one of the most difficult variable to model in atmospheric dynamic simulations. The misfit between InSAR and atmospheric models ratios can also be explained by lateral variations of troposphere stratification. The point chosen for the atmospheric model prediction may not be representative of the average troposphere stratification in the radar scene.

With these sources of errors in mind, we first need to validate the interferogram correction with the InSAR derived delay/elevation ratios. We define the seasonal average ratio, $S_{avg}^{MOD}(s)$, as the average over 10 consecutive years of the daily ratio prediction computed on 15-days sliding windows (black line on Fig. 11a, b, and c). The associated seasonal standard deviation is $\sigma(s)$. Fig. 11a–c shows that all InSAR derived ratios (crosses) fall within the interval $[S_{avg}^{MOD}(s) - 2\sigma(s); \ S_{avg}^{MOD}(s) + 2\sigma(s)]$

(grey lines), with a few exceptions, even during periods of low daily variability (in winter for Haiyuan or Afar areas). The distribution (or PDF) of InSAR derived ratios around the seasonal average, after normalization by $\sigma(s)$, $PDF_1[(S_i^{SAR} - S_{avg}^{MOD}(s)) / \sigma(s)]$ (black line on Fig. 11d–f), is only slightly larger (by less than 10%) than the distribution of the predicted daily variability around the seasonal average, $PDF_2[(S^{MOD} - S_{avg}^{MOD}(s))/ \sigma(s)]$ (grey line on Fig. 11(d–f)). Therefore, the variability of InSAR derived ratios can almost be completely explained by the daily climate variability alone, and is not clearly increased by errors on the estimation of InSAR derived ratios. This suggests that InSAR derived ratios are relatively well constrained and can be used to correct interferograms if they are not biased by deformation.

When InSAR derived ratios cannot be estimated due to a trade-off with the deformation pattern, shall we correct interferograms with the delay/elevation ratio predicted at acquisition dates, $S_i^{MOD}$, or with the seasonal average $S_{avg}^{MOD}(s)$? In other words, do global atmospheric models provide, beside the seasonal trend, a good estimate of the water vapor stratification for the daily fluctuations around the seasonal average? To answer this question, we also compute the distribution of InSAR derived ratios minus the delay/elevation ratio predicted at acquisition dates, $PDF_3[(S_i^{SAR} - S_i^{MOD})/\sigma(s)]$ (dark red line on Fig. 11d–f). For the Lake Mead test site or for the Haiyuan area, $PDF_3$ has a larger peak and a smaller width (decreased by a factor 1.3 and 2.5, respectively, Fig. 11) than $PDF_1$ comparing $S_i^{SAR}$ with the seasonal average $S_{avg}^{MOD}(s)$. This suggests that using the predicted ratio at the acquisition date is more efficient than using the average seasonal
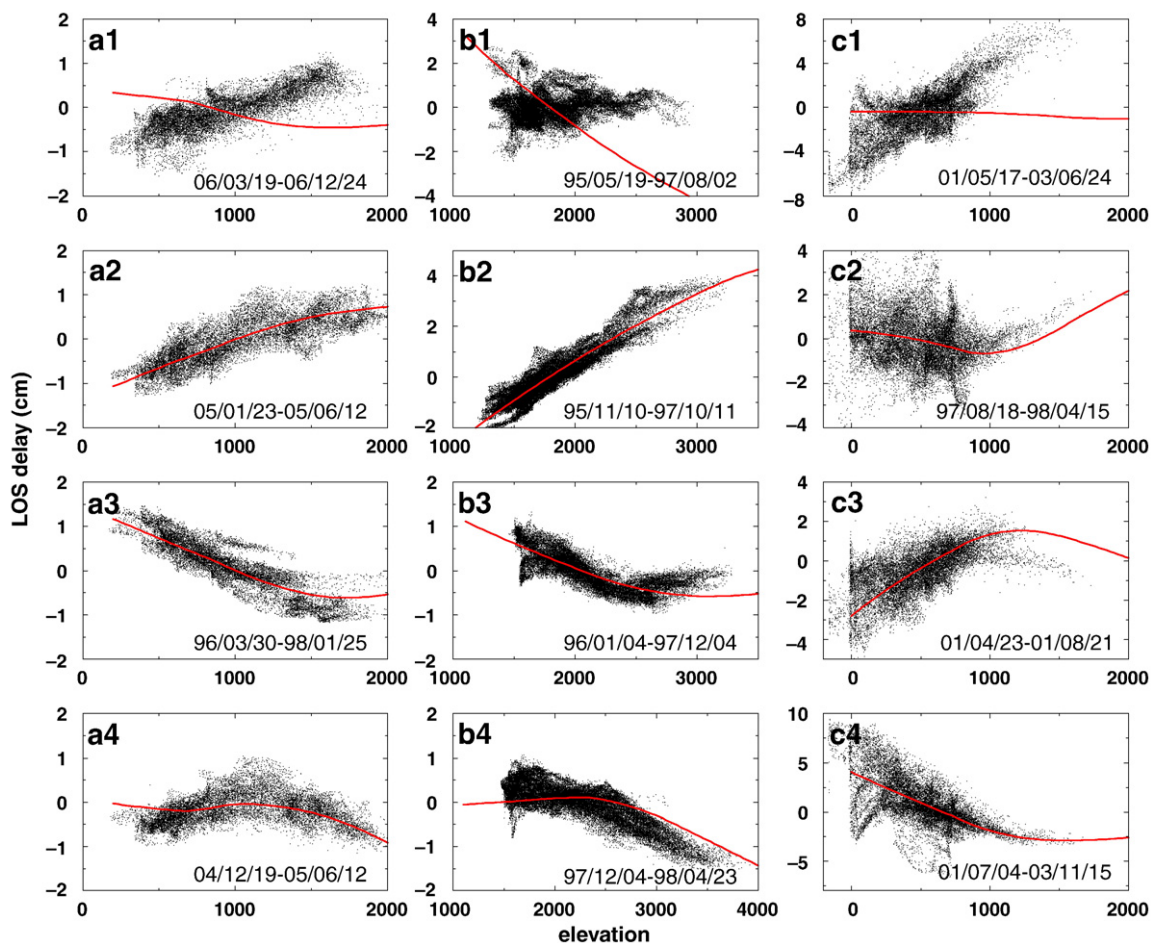


**Fig. 12.** Examples of single path LOS delay versus elevation plots for a few interferograms (black dots) and predicted by global atmospheric models (red line), in Lake Mead (column a), Haiyuan (column b), and Afar (column c) areas. Below the model surface elevation (680 m, 1750 m, and 500 m, respectively), the red curve is extrapolated. Note the much larger dispersion in the case of Afar. (For interpretation of the references to color in this figure legend, the reader is referred to the web version of this article.)

value. In Afar, $PDF_1$ and $PDF_3$ have the same width, suggesting that in this case ERA40/OPERA mostly predict the seasonal trend but hardly the daily fluctuations around it (Fig. 11f).

Finally, we can check on InSAR delay/elevation plots whether the stratified delay prediction at acquisition dates remains within the InSAR data scatter for all elevations. In a few cases (10 to 15% of interferograms covering the Lake Mead area), delay versus elevation relationships from interferograms are well defined while the stratified delay predicted by the global atmospheric models clearly deviates from them (see a few extreme examples on Fig. 12a1 and b1). Therefore, in such particular cases, we would tend to trust more InSAR derived delay/elevation ratios than atmospheric model predictions. However, in most cases, these models provide a good prediction of the delay/elevation relationship.

## 5. Non-linear phase to elevation relationships

We have shown above the good agreement between delay/ elevation ratios from atmospheric model predictions and InSAR derived ratios. The simple parameterization, based on the average delay/elevation ratio representative of the radar scene, allows a more robust estimate of the stratified delay from interferograms than using quadratic, cubic or exponential delay-elevation laws. The latter are indeed more sensitive to trade-offs between parameterized variables (e.g., between $z$ and $z^2$), turbulent delays, residual orbital errors or displacement field. Here, we first check the validity of the linear approximation by plotting the delay versus elevation derived from all available interferograms in the three test sites. The linear trend is most often well defined in the Lake Mead or Haiyuan areas (Fig. 2a and b). It is less frequently observed in Afar (Fig. 2c). Examples of clear non-linear delay to elevation relationships are displayed on Fig. 12. In Lake Mead area, a slight curvature can often be detected when turbulent atmospheric patterns have a small amplitude (Fig. 12a2). The curvature is seldom more pronounced (Fig. 12a3). Exceptionally, we observe a sign change in delay/elevation ratios between low and high elevation ranges (Fig. 12a4). In Haiyuan area, the curvature is often quite subtle (Fig. 12b2), with a few cases only displaying a clear change in delay/elevation ratios from low to high elevation ranges (Fig. 12b3 and b4). The small curvatures observed on Haiyuan plots may appear surprising given the high elevation and the large elevation range. In Afar, despite strong turbulent patterns and a limited elevation range, curvatures are detected in numerous interferograms. The InSAR delay/elevation ratio often changes importantly above ~900 m (Fig. 12c2, c3, c4). At low elevation, below 300 m, diverging trends are often present (Fig. 12c1, c4) which suggest a complex vertical stratification with large humidity concentration at low elevation at some acquisition dates, together with strong lateral heterogeneities.

The complete delay/elevation relationship for each interferogram can also be computed from global atmospheric models and Eq. (11) as $\delta L^s_{LOS}(z)_{ij} = \delta L^s_{LOS}(z)_j - \delta L^s_{LOS}(z)_i$, and is superimposed on InSAR delay-elevation plots with an adjusted constant delay shift (red lines in Fig. 12). The vertical resolution is low as there are only few ERA40 and OPERA pressure levels at low elevation. Furthermore, below the model surface elevation, curves are extrapolated using the values provided by the atmospheric models (note the trend below 680 m in Fig. 12a4). However, the difference between two dates $i$ and $j$ still evidences non-linear, more or less complex, shapes of $\delta L^s_{LOS}(z)_{ij}$ (Fig. 12). In overall, the comparison between the predicted delay/elevation relationship and the observed one is satisfactory, in the sense that the presence or absence of a significant curvature and its sign are well predicted for all three sites (Fig. 12a2–a4, b2–b4, c2–c4).

The curvature in delay to elevation relationships in interferograms is due to changes in the shape of this relationship from one acquisition to the other. Both the hydrostatic and the wet delay curvatures change with time. However, the amplitude of temporal hydrostatic curvature

variations, of ~4 cm/km$^2$, is relatively low and only explains a small part of the non-linear shapes observed at our three test sites. When the humid height scale, $H_v$, presents strong seasonal variations (as for Afar), non-linearities in the delay to elevation relationship are mostly controlled by the wet delay and are seasonal. In Afar, one can thus observe and predict an upward concavity for delay to elevation plots with a summer master date and a winter slave date, and inversely for interferograms between winter and summer (Fig. 12c2–c4).

## 6. Discussion and conclusion

In this paper, we recall the main equations useful to derive the stratified tropospheric delays in InSAR. We emphasize that the sensitivity of this delay to atmospheric variables differs from that in GPS. InSAR stratified delays are integrated from the minimum to the maximum elevations in the radar scene, while GPS delays are integrated from ground to satellite. We also clarify the expression of the hydrostatic delay, that must be taken into account when surface temperature varies by more than 10 °C during the year.

The delay-elevation ratio derived from InSAR at each acquisition date is validated by the predictions of global atmospheric models, without further need of calibration of electromagnetic constants or atmospheric models variables. Both predicted and observed delay/ elevation ratios show the same seasonal signal and the same daily climate variability around the seasonal curve. Discrepancies between predictions and observations remain large in the Afar test site, in which case the vertical water vapor distribution seems to be rather complex and partly heterogeneous in space. We suspect that the sea proximity and the large daily climate fluctuations make water vapor stratification modelling rather difficult there. Turbulent patterns, quantified by deviations from the delay/elevation trend, are also particularly large in Afar with respect to the Lake Mead or Haiyuan sites. However, global atmospheric models in Afar predict very well the seasonality of delay-elevation ratios.

When ground displacement must be retrieved with a subcentimeter accuracy, it appears essential to correct beforehand the interferograms from the stratified tropospheric signal. In particular, in the case where a limited number of uncorrected interferograms is stacked to obtain a ground velocity map, sampling bias could result in a residual, non negligible relationship between phase and elevation as in the Haiyuan study area. Also, when the ground motion presents a non-linear temporal evolution, its measurement from an uncorrected InSAR time series may be biased if the acquisition dates irregularly sample days with low or large delay-elevation ratios (Lake Mead case). Finally, because the stratified delay is not random in time but presents seasonal fluctuations, atmospheric seasonal signals remain in smoothed, uncorrected InSAR time series (Afar case).

The stratified delay correction may be applied either using InSAR derived delay/elevation ratios or using global atmospheric models predictions. Both kinds of correction allow to remove the sampling biases in the Haiyuan and Lake Mead cases and the seasonal curve in the Afar case. The standard deviation of the error, $\sigma_e$, associated to this correction at each acquisition date, may be set equal to the standard deviation, $\sigma(s)$, of daily climate fluctuations around the seasonal average. The correction error, $\sigma_e$, would thus depend on the time of the year, and would be conservative. However, it is lower than $\sigma(s)$ in areas of relatively simple vertical water vapor stratification, and of moderate turbulent atmospheric patterns, such as in the Haiyuan area.

From our work, it appears more accurate to correct interferograms with InSAR derived delay/elevation ratios than with global atmospheric models predictions. However, the latter can be the only one to be used if the correlation between elevation and displacement is large, as expected on volcanoes (e.g., Etna, Beauducel et al., 2000), on some fault segments (e.g., Altyn Tagh, Lasserre et al., 2007), or in subsident basins (e.g., Mexico City, Lopez et al., 2008). When the coherence is

bad, it might also be useful to correct wrapped interferograms from the stratified tropospheric delay before unwrapping, to reduce unwrapping errors (Pinel et al., 2008). Finally, it appears that global atmospheric models provide on overall a good prediction and thus a possible correction of non-linear delay-elevation relationships, which might be difficult to obtain in a robust way from the interferograms themselves.

Further improvements in the correction of stratified atmospheric delays should occur in the near future. A new global atmospheric reanalysis with improved model physics and humidity analysis will be released by ECMWF. A combination of global atmospheric model predictions with MERIS total water vapor estimates might also be particularly useful for correcting ENVISAT interferograms. Finally, meso-scale atmospheric simulations will improve as well, and could help understanding the origin of complex vertical stratification and systematic lateral heterogeneities. Combined with data assimilation, they appear as the most promising tools for correcting interferograms of atmospheric delays.

## Acknowledgments

## References

Askne, J., Nordius, H., 1987. Estimation of tropospheric delay for microwaves from surface weather data. Radio Sci. 22, 379–386.

Baby, H.B., Golé, P., Lavergnat, J., 1988. A model for the tropospheric excess path length of radio waves from surface meteorological measurement. Radio Sci. 23.

Bean, B.R., Dutton, E.J., 1968. Radio meteorology. New-York, Dover.

Beauducel, F., Briole, P., Froger, J.L., 2000. Volcano wide fringe in ERS SAR interferograms of etna: deformation or tropospheric effect? J. Geophys. Res. 105 (B7), 16,391–16,402.

Berardino, P., Fornaro, G., Lanari, R., Sansosti, E., 2002. A new algorithm for surface deformation monitoring based on small baseline differential SAR interferograms. IEEE Trans. Geosci. Remote Sens. 40, 2375–2383.

Bevis, M.S., Businger, S., Chiswell, S., Herring, T.A., Rocken, C., Anthes, R.A., Ware, R.H., 1994. GPS meteorology: Mapping zenith wet delays onto precipitable water. J. Appl. Meteorol. 33, 379–386.

Cavalié, O., Doin, M.P., Lasserre, C., Briole, P., 2007. Ground motion measurement in the Lake Mead area, Nevada, by differential synthetic aperture radar interferometry time series analysis: probing the lithosphere rheological structure. J. Geophys. Res. 112 (B3), B03403. doi:10.1029/2006JB004344.

Cavalié, O., Lasserre, C., Doin, M.P., Peltzer, G., Jianbao, S., Xiwei, X., Shen, Z.K., 2008. Measurement of interseismic strain across the Haiyuan fault (Gansu, China), by InSAR. Earth Planet. Sci. Lett. 275, 246–257. doi:10.1016/j.epsl.2008.07.057.

Davis, J.L., Herring, T.A., Shapiro, I.I., Rogers, A.E.E., Elgered, G., 1985. Geodesy by radio interferometry: effects of atmospheric modelling errors on estimates of baseline length. Radio Sci. 20, 1593–1607.

Delacourt, C., Briole, P., Achache, A., 1998. Tropospheric corrections of SAR interferograms with strong topography. Application to Etna. Geophys. Res. Lett. 25, 2849–2852.

Doubre, C., Peltzer, G., 2007. Fluid-controlled faulting process in the Asal rift, Djibouti, from 8-year radar interferometry observations. Geology 35 (1), 69–72. doi:10.1130/G23022A.1.

Elliott, J.R., Biggs, J., Parsons, B., Wright, T.J., 2008. InSAR slip rate determination on the Altyn Tagh Fault, northern Tibet, in the presence of topographically correlated atmospheric delays. Geophys. Res. Lett. 35 (L12309). doi:10.1029/2008GL033659.

Emardson, T.R., Simons, M., Webb, F.H., 2003. Neutral atmospheric delay in interferometric synthetic aperture radar applications: statistical description and mitigation. J. Geophys. Res. 108 (B5), 2231. doi:10.1029/2002JB001781.

Farr, T.G., Kobrick, M., 2000. Shuttle radar topography mission produces a wealth of data. Eos Trans. AGU 81 (48), 583–585.

Ferretti, A., Prati, C., Rocca, F., 2001. Permanent scatterers in SAR interferometry. IEEE Trans. Geosci. Remote Sens. 39 (1), 8–20.

Foster, J., Brooks, B., Cherubini, T., Shacat, C., Businger, S., Werner, C.L., 2006. Mitigating atmospheric noise for InSAR using a high resolution weather model. Geophys. Res. Lett. 33 (L16304). doi:10.1029/2006GL026781.

Gaudemer, Y., Tapponnier, P., Meyer, B., Peltzer, G., Guo, S., Chen, Z., Dai, H., Cifuentes, I., 1995. Partitioning of crustal slip between linked active faults in the eastern Qilian

Shan, and evidence for a major seismic gap, the "Tianzhu gap", on the western Haiyuan fault, Gansu (China). Geophys. J. Int. 120, 599–645.

Goldstein, R., 1995. Atmospheric limitations to repeat-track radar interferometry. Geophys. Res. Lett. 22, 2517–2520.

Gray, A.L., Mattar, K.E., Sofko, G., 2000. Influence of ionospheric electron density fluctuations on satellite radar interferometry. Geophys. Res. Lett. 27 (10), 1451–1454.

Hanssen, R. (Ed.), 2001. Radar Interferometry, Data Interpretation and Error Analysis. Kluwer Academic Publishers, p. 308.

Lasserre, C., et al., 1999. Postglacial left slip-rate and past occurrence of $M \geq 8$ earthquakes on the western Haiyuan fault, Gansu, China. J. Geophys. Res. 104, 17,633–17,651.

Lasserre, C., et al., 2007. Interseismic strain across the Altyn Tagh and Haiyuan faults at the northern edge of the Tibetan plateau, measured by space geodesy. in Geophysical Research Abstracts CDROM, vol. 9, p. 10102.

Li, Z., Muller, J.P., Cross, P., Fielding, E.J., 2005. Interferometric synthetic aperture radar (InSAR) atmospheric correction: GPS and Moderate Resolution Imaging Spectro-radiometer (MODIS), and InSAR integration. J. Geophys. Res. 110 (D20), 4651. doi:10.1029/2004JB003446.

Li, Z., Cross, P., Cross, P., Albert, P., Fischer, J., Bennartz, R., 2006a. Assessment of the potential of meris near-infrared water vapour products to correct ASAR interferometric measurements. International Journal of Remote Sensing 33. doi:10.1029/2005GL025299.

Li, Z., Fielding, E.J., Cross, P., Muller, J.P., 2006b. Interferometric synthetic aperture radar atmospheric correction: GPS topography-dependent turbulence model. J. Geophys. Res. 111, B02404. doi:10.1029/2005JB003711.

Li, Z., Fielding, E.J., Cross, P., Muller, J.P., 2006c. Interferometric synthetic aperture radar atmospheric correction: medium resolution imaging spectrometer and advanced synthetic aperture radar integration. Geophys. Res. Lett. 33. doi:10.1029/2005GL025299.

Lohman, R.B., Simons, M., 2005. Some thoughts on the use of InSAR data to constrain models of surface deformation: noise structure and data downsampling. Geochem. Geophys. Geosyst. 6. doi:10.1029/2004GC000841.

Lopez, J., Doin, M.P., Tupin, F., Briole, P., and Nicolas, J.M. (2008), Time series analysis of Mexico city subsidence constrained by radar interferometry, accepted to J. of Applied Geophysics.

Mattar, K., Gray, A.L., 2002. Reducing ionospheric electron density errors in satellite radar interferometry applications. Can. J. Remote Sens. 28 (4), 593–600.

Mesinger, F., et al., 2006. North American regional reanalysis. Bull. Am. Meteol. Soc. 87, 343–360.

Meyer, B., Tapponnier, P., Bourjot, L., Métivier, F., Gaudemer, Y., Peltzer, G., Guo, S., Chen, Z., 1998. Crustal thickening in Gansu–Qinghai, lithospheric mantle subduction, and oblique, strike-slip controlled growth of the Tibet Plateau. Geophys. J. Int. 135, 1–47.

Meyer, F., Bamler, R., Jakowski, N., Fritz, T., 2006. The potential of low-frequency SAR systems for mapping ionospheric TEC distributions. IEEE Trans. Geosci. Remote Sens. 3 (4), 560–564.

Peltzer, G., Doubre, C., 2007. Phase Propagation Delay and Ground Movement Signal in InSAR Time Series of Afar. Geophysical Research Abstracts, EGU General Assembly meeting, vol. 9.

Peltzer, G., Crampé, F., Hensley, S., Rosen, P., 2001. Transient strain accumulation and fault interaction in the Eastern California shear zone. Geology 29 (11), 975–978.

Pinel, V., Hooper, A., la Cruz-Reyna, S.D., Reyes-Davila, G., Doin, M.P., 2008. Study of the deformation field of two active Mexican stratovolcanoes (Popocatepetl and Colima volcano) by time series of InSAR data. Fringe Workshop Proceedings, ESA Special Publication SP-649.

Puyssegur, B., Michel, R., Avouac, J.P., 2007. Tropospheric phase delay in InSAR estimated from meteorological model and multispectral imagery. J. Geophys. Res. 111 (B12), 7166–7174.

Remy, D., Bonvalot, S., Briole, P., Murakami, M., 2003. Accurate measurement of tropospheric effects in volcanic areas from SAR interferometry data: application to Sakurajima volcano (Japan). Earth. Planet. Sci. Lett. 213, 299–310.

Rosen, P.A., Hensley, S., Peltzer, G., Simons, M., 2004. Updated repeat orbit interferometry package released. Eos Trans. AGU 85 (5), 47.

Scharroo, R., Visser, P.N.A.M., 1998. Precise orbit determination and gravity field improvement for the ERS satellites. J. Geophys. Res. 103 (C4), 8113–8127.

Schmidt, D.A., Bürgmann, R., 2003. Time-dependent land uplift and subsidence in the Santa Clara valley, California, from a large interferometric synthetic aperture radar data set. J. Geophys. Res. 108 (B9), 2416. doi:10.1029/2002JB002267.

Schmidt, D.A., Bürgmann, R., Nadeau, R.M., d'Alessio, M., 2005. Distribution of aseismic slip rate on the Hayward fault inferred from seismic and geodetic data. J. Geophys. Res. 110, B08406. doi:10.1029/2004JB003397.

Smith, E.K., Weintraub, S., 1953. The constants in the equation for atmospheric refractive index at radio frequencies. Proc. I.R.E. 41, 1035–1037.

Taylor, M., Peltzer, G., 2006. Current slip rates on conjugate strike-slip faults in central Tibet using synthetic aperture radar interferometry. J. Geophys. Res. 1113 (B12). doi:10.1029/2005JB004014.

Thayer, G.D., 1974. An improved equation for the radio refractive index of air. Radio Sci. 9, 803–807.

Uppala, S., Kållberg, P., Simmons, A., Andrae, U., 2005. The ERA-40 re-analysis. Q. J. R. Meteorol. Soc. 131, 2961–3012.

Vigny, C., Huchon, P., Ruegg, J., Khanbari, K., Asfaw, L., 2006. Confirmation of Arabia plate slow motion by new GPS data in Yemen. J. Geophys. Res. 111 (B02402). doi:10.1029/2004JB003229.

Wadge, C., et al., 2002. Atmospheric models, GPS and InSAR measurement of the tropospheric water vapour field over Mount Etna. Geophys. Res. Lett. 29 (19), 1905. doi:10.1029/2002GL015159.

Webley, P.W., Bingley, R.M., Dodson, A.H., Wadge, G., Waugh, S.J., James, I.N., 2002. Atmospheric water vapour correction to InSAR surface motion measurements on mountains: results from a dense GPS network on Mount Etna. Phy. Chem. Earth 27, 363–370.

Williams, S., Bock, Y., Pang, P., 1998. Integrated satellite interferometry: tropospheric noise, GPS estimates and implication for InSAR products. J. Geophys. Res. 103 (B11), 27,051–27,067.

Wright, T., Parsons, B., Fielding, E., 2001. Measurement of interseismic strain accumulation across the North Anatolian Fault by satellite radar interferometry. Geophys. Res. Lett. 28 (10), 2117–2120.

Zebker, H.A., Rosen, P.A., Hensley, S., 1997. Atmospheric effects in interferometric synthetic aperture radar surface deformation and topographic maps. J. Geophys. Res. 102 (B4), 7547–7563.